Università degli Studi di Padova

Dipartimento di Fisica e Astronomia "Galileo Galilei"

Master Degree in Physics of Data

Final Dissertation

SURFACE RADIATION BALANCE OF THE EAST ANTARCTIC PLATEAU

(Variations, tendencies and clouds role)

INTERNAL SUPERVISOR:
Prof. Alberto Garfagnini

EXTERNAL SUPERVISOR:
Dr. Angelo Lupi

CANDIDATE:
Rebecca Ghidoni

Academic Year 2021/2022

Abstract

Aim of this thesis is to examine the effects of clouds on the radiation at the ground level at Dome C, in Antarctica. This area is considered to be representative of the entire East Antarctic Plateau.
The thesis will examine the radiation at the site, both from the Sun and from the Earth, and how it interacts with the ice sheets that cover the entire continent.
In particular we will analyze the change of clouds presence in the past decade and how this relates to the climate of the region. Thanks to a specific algorithm it is actually possible to calculate the theoretical radiance in condition of perfect clear sky at every point of the planet. Confronting this results with the experimental data it is possible to find out how clouds flux variation has affected Antarctica. We will analyze over 10 years of data recorded at the Italian-French station Concordia in order to obtain suitable parametrization of the four components of irradiance in clear-sky conditions.

Acknowledgements

Contents

List of Figures

Chapter 1

Introduction

1.1 Radiation

Earth's climate is characterized by a variety of factors but one of the most important is probably the radiation budget of the Earth-atmosphere system[1]. It plays a fundamental role in determining the thermal conditions and the circulation of the atmosphere and the ocean. Especially in the polar areas, where snow-covered surfaces, ice sheets and glaciers typically reflect 75%-95% of the incoming solar radiation [2].

In atmospheric science, the radiation that comes from the Sun is divided in shortwaves, the wavelength band that carries most of the energy associated with solar radiation, and longwaves, the band that encompasses most of the Earth-emitted radiation.

Considering the wavelength interval between λ and $\lambda + d\lambda$, that in the time interval dt crosses an element of area dA, in directions limited to the differential solid angle $d\Omega$, which is oriented to an angle θ with respect to the normal to dA [Figure 1.1] we have the radiant energy dE_λ. This energy

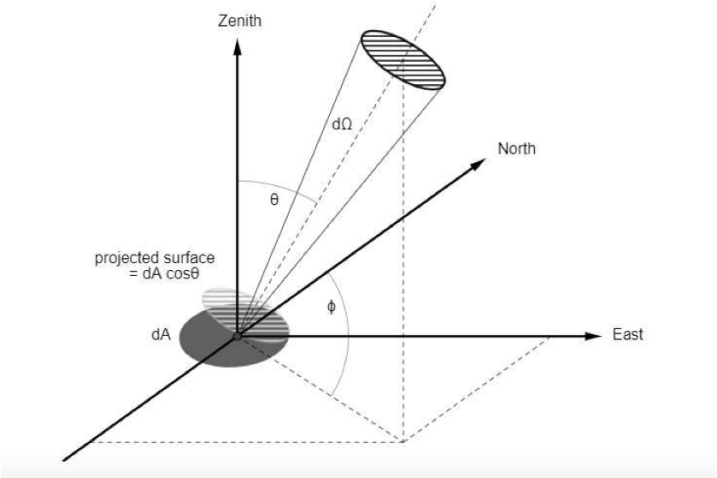

Figure 1.1: Coordinate system with zenith θ and azimuth ϕ angle and projection of the surface dA identified by a widespread object in a given direction from the plane

is expressed in terms of the monochromatic intensity, or radiance, I_λ :

$$dE_\lambda = I_\lambda cos(\theta) dA d\Omega d\lambda d\theta. \tag{1.1}$$

The monochromatic irradiance is defined as the normal component of I_λ integrated over an hemispheric solid angle:

$$F_\lambda = \int_\Omega I_\lambda cos(\theta) d\Omega = \int_0^{2\pi} \int_0^{\frac{\pi}{2}} I_\lambda cos(\theta) sin(\theta) d\theta d\phi \tag{1.2}$$

That for isotropic radiation results to $F_\lambda = \pi I_\lambda$. The total irradiance, F, is obtained integrating over the entire electromagnetic spectrum:

$$F = \int_0^\infty F_\lambda d\lambda \tag{1.3}$$

and it is measured in $\frac{W}{m^2}$.

The solar constant S_0 is defined as the energy per unit time which crosses a surface of unit area normal to the solar beam at the mean distance between the Sun and the Earth and it represents the total energy reaching the top of the atmosphere. According to energy conservation principle, the energy emitted from the Sun remains constant between the Sun and the Earth, due to the fact that there is no medium between the two. So on the top of the atmosphere of the Earth we have:

$$S_0 = \frac{W_0}{4\pi r^2} = \frac{F 4\pi a_s^2}{4\pi r^2} \tag{1.4}$$

where a_s is the radius of the Sun and r is the mean Earth-Sun distance. Thus the solar constant can be expressed as:

$$S_0 = F \left(\frac{a_s}{r}\right)^2 \tag{1.5}$$

The solar constant value, $S_0 = 1366 \pm 3 \ \frac{W}{m^2}$, is defined for the mean distance between the Earth and the Sun, $d_m = 1.496 \cdot 10^{11}$m. The maximum distance between the Sun and the Earth ($1.521 \cdot 10^{11}$m) is called aphelion and the Earth is in this position at the beginning of July. The point of minimum distance ($1.471 \cdot 10^{11}$ m) is called perihelion, and it happens at beginning of January. So it is necessary to add a $(d_m/d)^2$ Sun-Earth distance correction, that it is usually designated with AU. Considering the very low eccentricity of the Earth, the AU value slightly oscillates around 1, with variations less than 0.017.

The irradiance on an horizontal surface at the top of the atmosphere also depends on the sun zenith angle:

$$F_h = F cos\theta = S_0 \left(\frac{d_m}{d}\right)^2 cos\theta \tag{1.6}$$

where F, equation (1.3), is the irradiance on a plane normal to the solar beam and θ is the latitude.

When the solar radiation hits the Earth's atmosphere it is absorbed and scattered by atmospheric gases, aerosols, clouds, and, in the end, by the Earth's surface. Atmospheric scattering is due to particles of different size, like gas molecules ($\sim 10^4 \mu m$), aerosols ($\sim 1\ m$), water droplets ($\sim 10 \mu m$), or rain drops ($\sim 1 cm$). For spherical particles, of radius a, we can define the so called size parameter $x = \frac{2\pi a}{\lambda}$.

If $x << 1$ (particle small compared with the wavelength), the scattering is called Rayleigh scattering. An example is the scattering of visible light by atmospheric molecules. If $x \approx 1$ (particle has about the same size as the wavelength) the scattering is called Lorenz-Mie scattering. If $x >> 1$ (particle large compared with the wavelength) the scattering is called geometric scattering, and it can be studied by using geometrical optics. For low densities of molecules and particles in the air, the scattering is independent, i.e. each particle scatters radiation as if the other particles did not exist. When density increases, like inside the clouds, each particle can scatter the radiation that has been already scattered by other particles. This process is called multiple scattering.

1.1.1 Rayleigh scattering

The description of the interaction between sunlight and air molecules is due to Rayleigh [3]: Rayleigh considered a molecule exposed to electromagnetic radiation as an oscillating dipole, that, interacting with the wave's electromagnetic field, radiates a scattered wave. The scattered intensity is propor-

tional to the magnitude of the electric field E of the scattered wave, that at large distances from the dipole behaves as a plane wave, and can be expressed as:

$$I(\Theta, r) = I_0 k^4 \frac{\alpha^2}{r^2} \frac{(1 + cos^2\Theta)}{2} \tag{1.7}$$

where I_0 is the intensity of the incident sunlight, θ is the scattering direction, r is the distance from the radiating dipole, k is the wavenumber, α is the polarizability of the scatterer. Considering the wavelength $\lambda = \frac{2\pi}{k}$ and a phase function

$$P(\Theta) = \frac{3}{4}(1 + cos^2\Theta) \tag{1.8}$$

we can rewrite equation (1.7) as :

$$I(\Theta, r) = I_0 \frac{\alpha^2}{r^2} \frac{32\pi^4}{3\lambda^4} P(\Theta) \tag{1.9}$$

The scattered intensity has a maxima in the forward ($\Theta = 0°$) and backward ($\Theta = 180°$) directions, with equal energy directed into each halfspace.

We define the refracting index as:

$$m = m_r - m_i \tag{1.10}$$

where m_r is the real part, related to the phase speed of the electromagnetic radiation in a medium, and m_i is the imaginary part, related to its absorption, relative to those in a vacuum

At visible wavelengths the absorption by air molecules is small enough for m_i to be ignored, so the fraction of the scattered power over the incident flux for an individual molecule, called scattering cross section, is given by:

$$\widehat{\sigma} = \frac{32\pi^3(m_r - 1)^2}{3n^2\lambda^4} \tag{1.11}$$

where n is the number density of the molecule.

1.1.2 Lorentz-Mie scattering

Mie treatement of scattering [4] applies to the interaction of radiation with aerosol and cloud droplets. The real refractive index for water, $m_r(\lambda)$, is of the order of unity, but varies slightly with wavelength while the imaginary refractive index $m_i(\lambda)$ is proportional to the absorption coefficient and is small in the visible domain, but sharply increases for $\lambda > 1\mu m$, making clouds optically thick in the IR.

Mie scattering possesses a much stronger directionality compared to that of Rayleigh. It exhibits a strong forward scattering, expecially at shorter wavelenght, which are sharply peaked about $\Theta = 0$ and for which absorption is small; a weaker maximum appears for backward scattering for wavelengths in the near-IR and visible regions.

The mean extinction cross section, the area that, when multiplied by the irradiance of the incident electromagnetic waves , gives the total scattered and absorbed radiant flux , for the particle population is nearly constant across the visible, where cloud droplets are large, and the extinction is only due to scattering, that is wavelength independent: individual components of sunlight are then scattered with equal efficiency, therefore clouds appear white. The extinction cross section attains a maximum near 5μm, wavelength comparable to the mean radius of cloud droplets, and falls off at longer wavelengths. Scattering dominates over absorption at wavelengths of SW radiation. Exceptional are narrow bands at $\lambda \simeq 3$ and 6 μm, where the absorption spectra of water and ice are peaked.

1.1.3 Absorption

In atmospheric science absorption is defined as the conversion of radiation in another form of energy, like heat, due to atmospheric molecules or aerosols.

The UV radiation in the interval $0.2-0.3$ μm is absorbed in the stratosphere [Figure 1.2], mainly by O_3. Radiation with λ shorter than 0.2 μm is absorbed by O_2 , N_2 , O and N. Solar radiation is absorbed in the VIS and IR in the stratosphere, mainly by H_2O, CO_2 , O_2 and O_3 .

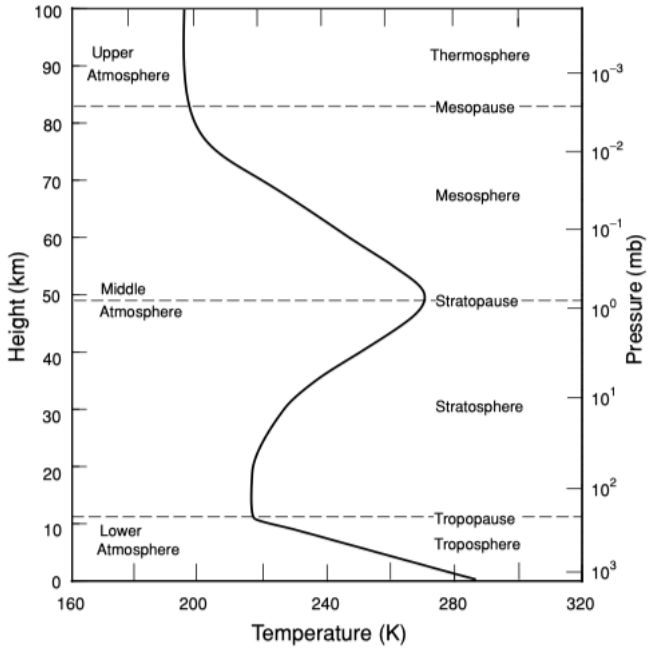

Figure 1.2: Mean profile of Earth's Atmospheric temperature

Scattering and absorption are usually associated. Both processes remove energy from incident radiation, and this attenuation is called extinction.

The angular distribution of light intensity scattered at a given wavelength is called phase function, P. If θ is the scattering angle, i.e. the angle between the incident and scattered waves, P is the ratio between the intensity scattered at the angle θ and the total scattered intensity. P is defined so that its integral over the unit sphere centered on the scattering particle is 4π:

$$\int_0^{2\pi} P(\Theta) sin\Theta d\Theta d\phi = 4\pi \tag{1.12}$$

1.2 Albedo

Albedo is a physical parameter that describe the ratio between the radiant energy received from the Sun and the one reflected and diffused from the planet's surface back into space. The entire reflected light discussion is possible since the Earth is not a perfect black body.
The ground albedo strongly depends on the nature of the surface [Figure 1.3], and on the spectral and angular distribution of the incoming radiation. Broadband albedo can be expressed as:

$$\alpha = \frac{F_{\uparrow}}{F_{\downarrow}} \tag{1.13}$$

where $F_{\uparrow}$ is the reflected radiative flux and $F_{\uparrow}$ the incident one. Albedo varies between 0 and 1, where the first value corresponds to a a black body that absorbs all incident radiation and the second to a body that reflects it all. Such reflection is influenced either by the nature of the surface or by the angular distribution of the incoming radiation. In Antarctica the study of the albedo allows us to determine some crucial moments during the year.

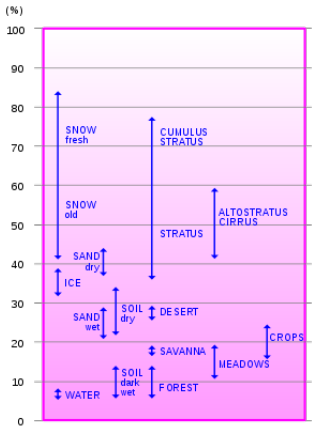

Figure 1.3: Albedo vaues for different surfaces.
Image from *https://en.wikipedia.org/wiki/Albedo*

1.3 Radiative transfer in presence of clouds

The presence of liquid and solid particles greatly elongates the path traveled by the photons of shortwave radiation, which then undergo repeated reflection and diffraction. Along with absorption inside particles, this sharply increases the optical depth posed to incident radiation. The radiative transfer equation for monochromatic radiation of intensity I_λ crossing a layer of thickness ds and density ρ , has the following general form:

$$\frac{dI_\lambda}{\rho k_\lambda ds} = -I_\lambda + J_\lambda \tag{1.14}$$

where J_λ is the source function, that describes the contribution of the emission of the layer to the resulting intensity. In absence of scattering, under local thermodynamic equilibrium conditions, the source function is given by the Planck function $B_\lambda(T)$. In presence of scattering, that cannot be neglected in presence of a cloud, it becomes:

$$\begin{aligned} J(\phi,\mu,\tau) = \frac{\omega}{4\pi}\int_0^{2\pi}\int_{-1}^{1} I(\phi',\mu',\tau)P(\phi,\mu;\phi',\mu')d\phi' d\mu' + \\ + \frac{\omega}{4\pi}F_\odot P(\mu,\phi;-\mu_0,\phi_0)e^{\frac{\tau}{\mu_0}} + (1-\omega)B[T(\tau)] \end{aligned} \tag{1.15}$$

where $\mu = cos\theta$, ϕ is the azimuth, τ is the optical depth, ω is the single scattering albedo; the wavelength dependence is implicit and emission is ignored. The fist term on the right-hand side represents the contributions to diffuse radiation from multiple scattering of the diffuse intensity I, whereas the second term represents the contribution from single scattering of direct solar radiation I_s .
The radiative transfer equation becomes much more complicated in presence of scattering[5].

The obtained solution for scattered irradiance can be used to evaluate the cloud albedo and trasmissivity in presence of a cloud. At visible wavelengths,

cloud albedo increases sharply at small optical depth and reaches a constant value of 0.8 for high optical depth; even shallow stratus are highly reflective. Transmissivity presents an opposite trend, i.e. it decreases with increasing τ_c. The two quantities are nearly complementar, so that most of the incident SW is reflected or transmitted, and only a 10% is absorbed. Moreover, α_c increases with increasing solar zenith angle, as it elongates the slant optical path; the opposite trend is observed for t_c . Shallower clouds depend even more strongly on solar zenith angle because the slant optical path then varies between optically thin and optically thick conditions.

Furthermore, for the same liquid water content, clouds with small droplets (i.e. continental clouds) have an higher albedo and smaller absorptivity than clouds with larger droplets, due to increased number densities; precipitation, on the other hand, sharply increases the absorptivity of clouds. Ice clouds are likewise highly reflective across the visible.

To understand the effect of clouds on longwave radiation we consider a simplified situation in which the monochromatic radiative flux (10 μm) interacts with an homogeneous optically thick scattering layer in radiative-convective equilibrium. First of all, an increase in surface temperature occurs. Under the cloud, there is a sharp change of downwelling and upwelling longwave radiative fluxes, both increasing from their clear-sky values. As the cloud is optically thick, in its interior the two fluxes undergo an adjustment that drives them nearly into coincidence. Changes in radiative fluxes also introduce strong warming and cooling in thin layers at the base and at the top of the cloud layer.

Chapter 2

Site and Instruments

2.1 Antarctica

Antarctica is Earth's southernmost continent. Situated almost entirely south of the Antarctic Circle and surrounded by the Southern Ocean, it contains the geographic South Pole. Antarctica covers more than 14.2 million km^2, making it the fifth-largest continent. The coastline is almost 18,000 km long. Antarctica is on average the coldest, driest, and windiest of the continents, and has the highest average elevation. It is mainly a polar desert, with annual precipitation of 200 mm along the coast and far less inland. The typical climate of the Antarctic plateau is cold and dry, with weaker winds and clearer skies with respect to the coastal region. Its extreme temperatures result from its latitude and altitude: for three months per year no solar radiation arrives (Polar Winter), and during the Summer, as the surface is covered with snow, more radiation is reflected than absorbed.

Dome C (75° 06' 00" S 123° 20' 00" E) is a summit on the Antarctic Plateau, 1220 km far from coast, and has an altitude of 3233 m a.s.l [Figure 2.1]. At Dome C, since 2005, the third permanent station of the Antarctic

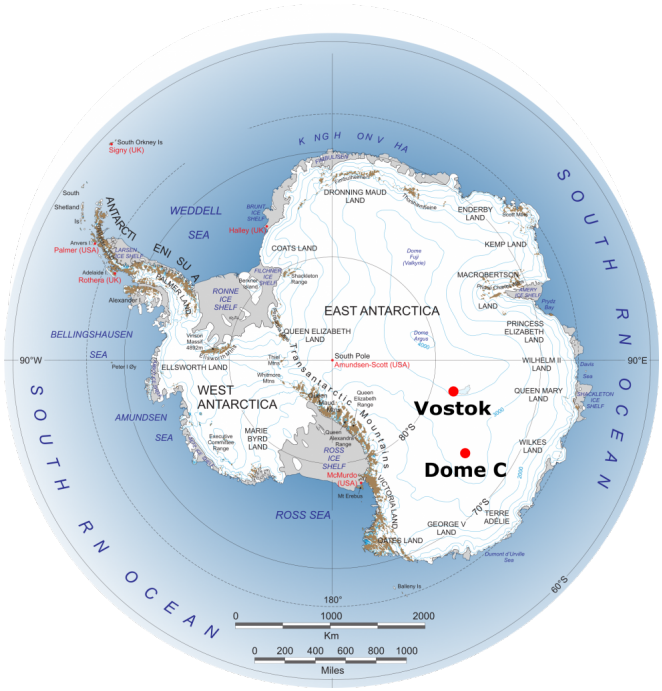

Figure 2.1: Location of Dome C in Antarctica.
Image from *http://berkeleyearth.org*

Plateu, the italian-french station Concordia, has been operative also during Austral Winter, making possible nighttime observations. The scientific importance of Concordia station is certified by the great number of international projects hosted in almost every sector of environmental science and astronomy.

In figure 2.2 the average daily trend of temperature divided by month is shown. In the graph all the data are reported in Greenwich Mean Time (GMT), while Antartica has a Local Time (LT) of 8 hours more [GMT + 8:00].

Winter months do not present a daily cycle, as expected as a consequence of the absence of the Sun, and temperature remains fairly constant around $-65°C$. In April and September the Sun is above the horizon just for some hour every day and we can observe a small rise in the daily temperature profile; this effect becomes more evident in October and March. During the remaining four months the daylight hours are 24 so a typical diurnal cycle sets up, with minimum temperature reached between 3:00 and 4:00 and maximum occurring around 15:00: these times of the day do not correspond to minimum and maximum insolation hours, as a certain time span is required for the snow to cool down and heat up. There is a difference of almost $15°C$ between December-January and November- February daily curves: this is a consequence of the minor amount of incoming solar radiation, as it depends on the the solar zenith angle, which is lower in December and January.

In figure 2.3 the monthly and yearly averages of temperature are showed. A well defined yearly cycle is visible, with maxima that slightly exceed $-30°C$ taking place in January and in December and minima falling between $-70°C$ and $-60°C$ occurring in August: the thermal excursion oscillates between $35°C$ and $40°C$. The overall trend throughout the years is quite constant just under $-50°C$, with a peak in 2014 due to an absence of data in the winter of that year.

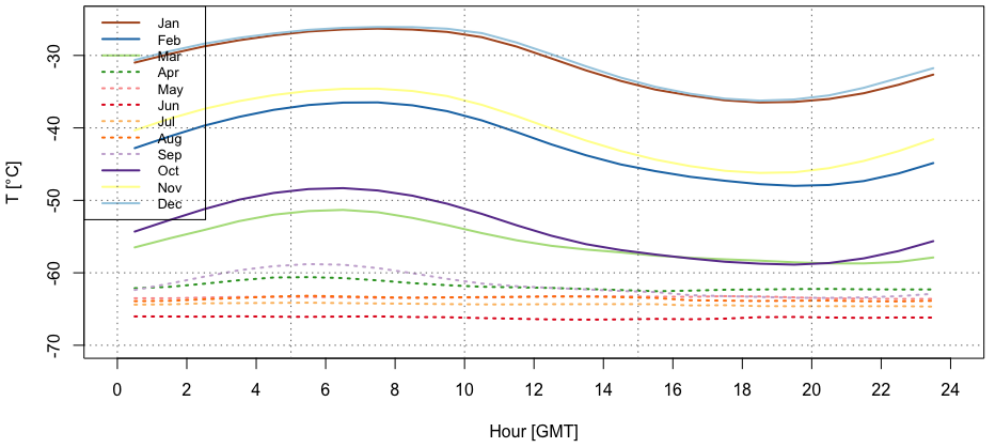

Figure 2.2: Mean daily curves of temperature for every month. Different colours are used to distinguish seasons.

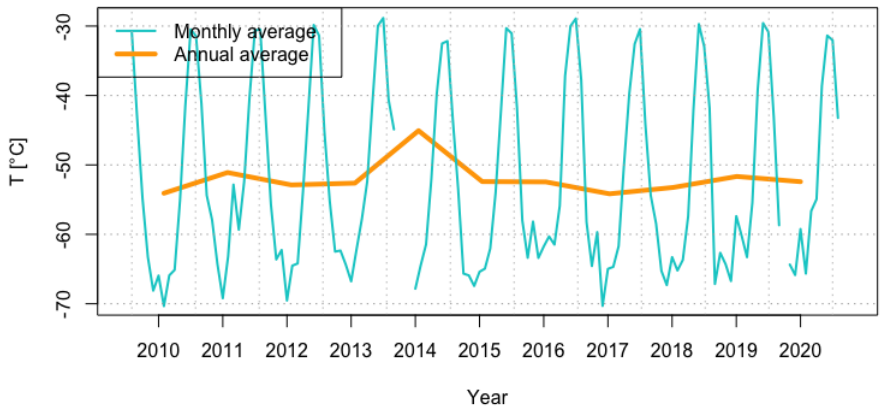

Figure 2.3: Time Series of monthly (cyan line) and annual (orange line) mean of atmospheric temperature at Dome C between Jenuary 2010 and February 2021

2.2 Temperature record

Despite the mean temperature has not significantly changed in the last decade, there were some significant variations compared to the average. For example in March 2022 there has been detected the maximum temperature ever [Figure 2.4].

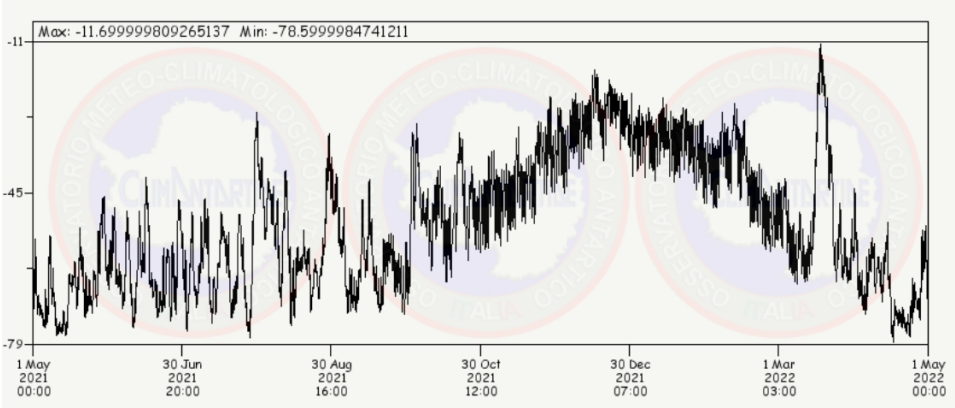

Figure 2.4: Air temperature at Dome C in the period from 2021-05-01 to 2022-04-30. It is possible to see the peak in March 2022. Figure from *https://www.climantartide.it/dataonline/aws*

.

2.3 Clouds observations in Antarctica

In the Polar regions clouds act as a critical forcing factor on the radiation budgets at the top of the atmosphere and the surface. In the Antarctic, cloud observations have largely been confined to synoptic observations, although in recent years these measurements have been supplemented by occasional in situ microphysical measurements, mainly of low cloud from the surface, and

radiometric measurements made from the surface and from satellite data. These measurements have only been made at a few locations and these locations may not be representative of the continent as a whole. It is not easy to model the relation between radiative balance at the surface to cloud properties. Thus, observational data are crucial, expecially in peculiar areas where the sensitivity of the surface-atmosphere system to clouds is more pronounced, in order to improve the parametrization schemes to be inserted in climatic models and test their results.

Several methods have been used to measure cloud cover in the Antarctic (ground-based visual observations, satellite measurements, active measurements such as LIDAR (Light Detection and Ranging o Laser Imaging Detection and Ranging)[[6]]). These methods can give quite different results, and it can be difficult to establish the true value of the extent and frequency of cloud. Surface visual observations have been routinely made at Antarctic research stations for the last 50 years, and give the longest running cloud data set available [7]. However, the surface observing sites are widely spaced in Antarctica, and most are located close to the coast. Visual observations are subjective, and changes in observer can result in step changes in particular measurements. Also, visual observations during the night are difficult to make because of the low level of illumination of the clouds and this is particularly true of Antarctic clouds during the winter.

Surface radiation measurements can also be used to derive cloud cover.

The best measurements are those retrieved from surface-based pyrgeometer measurements, both in terms of accuracy and length of record, as they are not affected by the lack of sunlight[8]. Comparing surface visual observations with values retrieved from the pyrgeometer, it is possible to show that during summer the two values agree well, whereas during winter the visual observations are around 20% lower[8]. The pyrgeometer values suggest that the cloud cover at the South Pole is constant throughout the year, at around

50-60%.

Passive satellite instruments measure the upwelling radiation emitted from the surface or atmosphere, and measurements taken using such instruments have a much better spatial coverage. With passive measurements it can be difficult to distinguish between the clouds and the underlying snow surface, as the temperature and radiative properties of the cloud and snow surface are similar.

The best surface observations suggest that the fractional cloud cover at the South Pole is around 50-60% in all seasons, whereas the cloud cover rises to around 80-90% close to the coast of the continent. Microphysical observations of cloud parameters are also very sparse in the Antarctic. However, the few measurements that do exist show predominantly ice-crystal clouds across the interior, with mixed-phase clouds close to the coasts. A wide range of crystal shapes is observed at all sites [9].

A predominance of thin cirrus clouds is on average observed on the Antarctic coast [10], with larger crystals observed in summer than in winter, larger optical depths in summer than in winter and larger optical depths at the coast than in the interior; these results conform to expectations, because the atmosphere contains more water vapor at the coast than in the interior and more water vapor in summer than in winter. Also, are pointed out the large difficulties encoutered in measure surface albedo, which is strongly coupled with cloud effects over highly reflective surfaces because of multiple reflections between cloud base and the surface, and so presents high uncertainties.

Typical antarctic atmospheric phenomena comprehend blowing snow, i.e. snow particles lifted from the surface by the wind, diamond dust, i.e. small ice crystals forming in the persistent temperature inversion layer, particularly strong during winter, and snow grains, i.e. larger ice crystals falling from clouds, more common in the coastal region.

2.4 BSRN

Baseline Surface Radiation Network (BSRN) began its work in 1992 with 9 stations distributed globally, including the Antarctic, Arctic, Atlantic and Pacific oceans, North America, Africa and Europe. Currently (status 2018-01-01), the network comprises 59 stations (delivering data to the archive) and 9 candidates (stations recently accepted into the network with data forthcoming to the archive), collectively representing all seven continents as well as island-based stations in the Pacific, Atlantic, Indian and Arctic oceans. Each BSRN station is committed to measuring at least the following radiation fluxes (SI unit $\frac{W}{m^2}$) continuously in high temporal resolution (about 1Hz) and providing quality-tested means for 1 minute intervals (with the time stamp of the datapoint represent- ing the starting point of the 1 min average). The ISP-CNR (Institute of Polar Sciences-CNR) manages this observatory at the Italian-French Concordia station in Antarctica. Installed in 2006, the BSRN was funded by the PNRA [Programma Nazionale di Ricerche in Antartide] and consists of a series of passive instruments (radiometers and photometers) that measure different components of the radiation balance (both in the solar and infrared spectrum), includingthe surface albedo.

2.5 Instruments

As all the BSRN stations at Dome C continuous measurements of broadband surface irradiance, 0.3-3 μm for the solar radiation and the band 3-50 μm for longwave radiation, are carried on with a 1-minute rate. Radiation measurements are performed through:

- PYRANOMETER: used to measure global solar radiation, so it has a fiel of view ofof 180°, to respond both to the direct solar beam and to

diffuse sky radiation from the whole hemisphere . The sensing element is a thermopile with a black coating and is covered with a quartz dome with transmittance that approaches unity in the visible and near IR wavelength range (0.3-3 μm); there is also a glass shield, to isolate the sensor from the environment, and a fan, to avoid heating,

- PYRGEOMETER: used to measure longwave radiation in region between 3-50 μm. In this case there is a flat silicon window to isolate the sensing element from the environment, and to filter only IR radiation,

- PYRHELIOMETER: used to measure the direct solar beam thanks to a thermal detector. It must be kept normal to the solar beam so is pointed at the Sun through a tracking mechanism. Its field of view is small (5°) in order to exclude the scattered sky radiation.

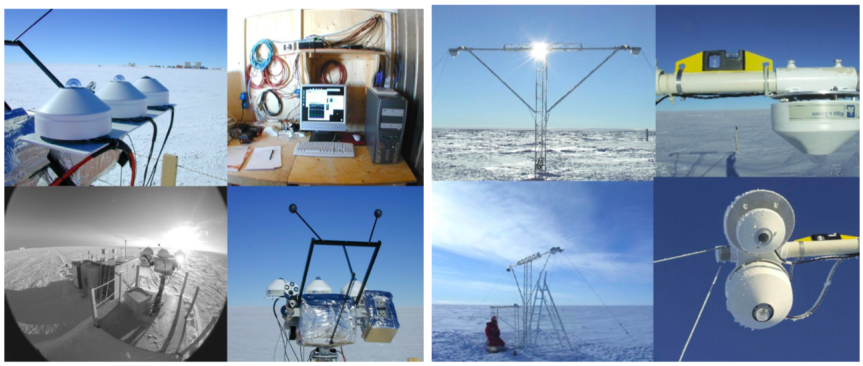

Figure 2.5: Instrumental set up at Dome C. On the left are shown the devices for downwelling irradiance measurement, on the right the albedo rack for upwelling irradiance measurements.

At Dome C downwlling components are measured since the end of 2005, while upwelling components are measured since the begining of 2007. Measure of diffuse and downwelling longwave radiation are performed with shadowbands on the radiometers. For what concerns the upwelling measurements

of shortwave radiation, two CM22 have been located on the opposite sites of the albedo rack.

2.6 Quality check and quality assurance

BSRN ensure the quality of all their data. Every measurment needs to pass a quality check[11]. Signals are acquired by a datalogger (Campbell) every second and the 1-minute average along with standard deviation, minimum and maximum values represent the raw data obtained from the measurement system. These 1-minute raw data are corrected following BSRN guidelines [12], in order to eliminate instrumental errors. The quality check ensures that irradiance measurements fall between certain limits (divided in physical possible limits, PPL, and extremely rare limits, ERL) and satisfy certain intercomparison criteria:

Quantity	ERL		PPL	
	Min$[\frac{W}{m^2}]$	Max$[\frac{W}{m^2}]$	Min$[\frac{W}{m^2}]$	Max$[\frac{W}{m^2}]$
Global(SWD)	-2	$S_a \cdot 1.2 \cdot \mu_0^{1.2} + 50$	-4	$S_a \cdot 1.5 \cdot \mu_0^{1.2} + 100$
Diffuse(DIF)	-2	$S_a \cdot 0.95 \cdot \mu_0^{1.2} + 10$	-4	$S_a \cdot 0.95 \cdot \mu_0^{1.2} + 50$
Direct normal(DIR)	-2	$S_a \cdot 0.95 \cdot \mu_0^{0.2} + 10$	-4	S_a
Longwave down(LWD)	60	500	40	700

Parameter	Min	Max	Restriction to data
SWD/SUM	0.92	1.08	SZA $< 75°$ and SUM $> 50\frac{W}{m^2}$
SWD/SUM	0.85	1.15	$75° <$ SZA $> 93°$ and SUM $> 50\frac{W}{m^2}$
DIF/SWD	-	1.05	SZA $< 75°$ and SWD $> 50\frac{W}{m^2}$
DIF/SUM	-	1.10	$75° <$ SZA $> 93°$ and SUM $> 50\frac{W}{m^2}$
LWD	$0.4 \cdot \sigma \cdot T_a^4$	$\sigma \cdot T_a^4 + 25\frac{W}{m^2}$	-

In the above tableof parameters the meaning varibles are:

1. SZA: solar zenit angle,
2. μ_0: cos(SZA),
3. S_a: $\frac{S_0}{AU}$ with $S_0 = 1366\frac{W}{m^2}$ and AU=normalized sun-earth distance,
4. SUM: μ_0·DIR + DIF,
5. T_a: Air temperature (K),
6. σ: Stefan-Boltzmann constant.

Another test concerns the k-space. Various studies (e.g., [13],[14]) have defined a number of tests for physical limits and to detect possible tracker issues. These tests are based on the clearness indices K_n , K, and K_t , and their physical relationships. These quantities are defined as:

- $K_n = \frac{DNI}{ETN}$
- $K = \frac{DIF}{GHI}$
- $K_t = \frac{GHI}{ETN*cos(SZA)}$

where ETN is the extraterrestrial irradiance at normal incidence, and SZA is the solar zenith angle. A visual inspection [Figure 2.6] of the time series of irradiances' components, in combinations with other information, has been performed, being considered the most effective test [15]. The test has been performed on the data from the SPN1 sensors:

- a): visualization of the deviation of the pyrheliometer's DNI from the DNI calculated from DIF and GHI (i.e., closure error). As expected most of the data are near 0, meaning that the calculated DNI is very similar to the measured one,

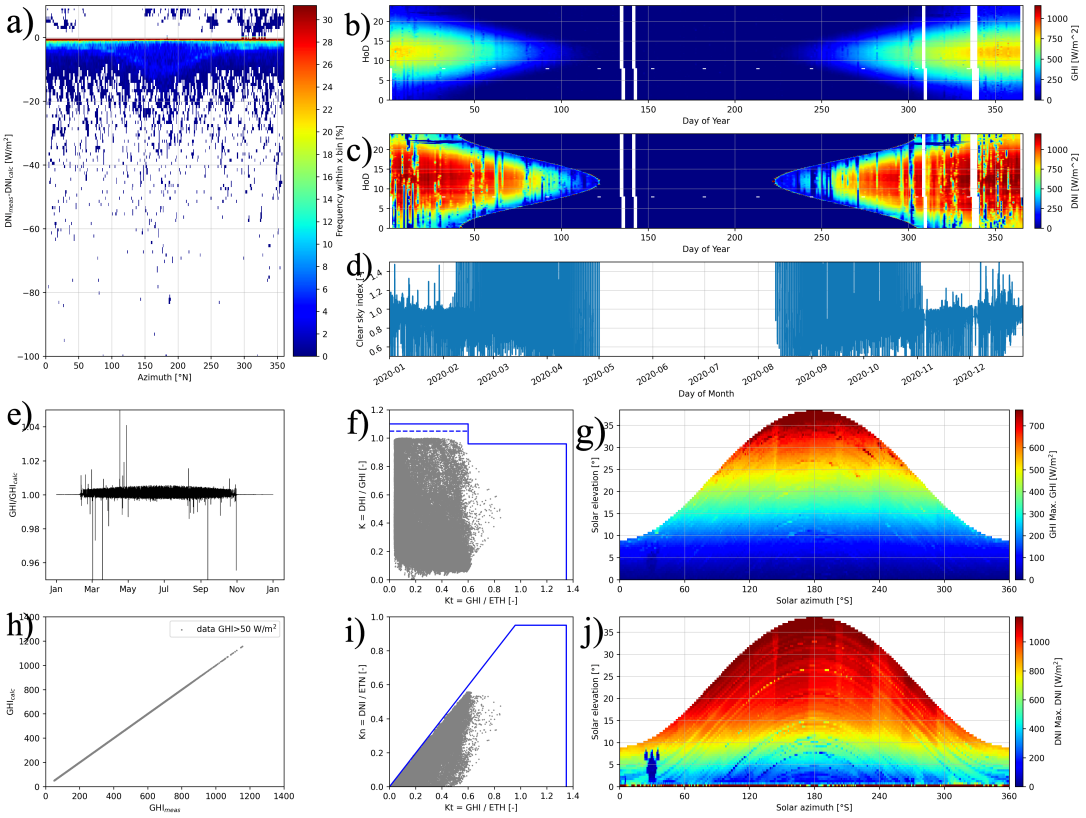

Figure 2.6: Result of quality check on the data of 2020

- b) and c) and g) and j): an overview of the diurnal variation of DNI and GHI as a function of time, in Local Time, and solar position. In the winter months (June, July and August) the radiation is null for both the components of the sunrays. For the rest of the year the components present the maximum at noon and and a symmetrical decrease in the morning and in the afternoon. In j) it is also possible to see the shadow of the measuring tower,

- d): daily ratio between real global shortwave irradiance and the radiation in perfect clear sky conditions. As in b) and c) there is no results for the winter months. In Spring and Autumn the ratio is very noisy, due to the small data sample. In summer the ratio becomes more stable around 1,

- e) and h): a comparison of the pyranometer GHI measurement to the GHI calculated from DNI and DIF. In e) we can observe that the calculated GHI is slightly higher than the measured one with the most significant variations in the winter months, when we have less data,

- f) and i): visualization of the data points in K-space with the applied limits (blue lines). We can see that all the data respect the physical limits.

Chapter 3

Radiation

3.1 Radiation in Antarctica

After the quality check we are finally ready to analize the cleaned data. The first analysis is done on the four components of irradiance: shortwave upwelling and downwelling irradiance ($F_{\uparrow,SW}$ and $F_{\downarrow,SW}$), and longwave upwelling and downwelling irradiance ($F_{\uparrow,LW}$ and $F_{\downarrow,LW}$). Every point is a daily mean performed on all the 1-minute data of that day from the different years.

It is easy to note how the zenit angle, i.e. the Sun elevetion, is the main controlling factor of shortwave irradiance tendency: its value is zero from May to the first week of August, when the yearly last sunset and first sunrise occurr while, for the rest of the year, the average irradiance is proportional to $cos(\overline{\theta})$, where $\overline{\theta}$ is the daily average value of the solar zenit angle (the minimum value of the solar zenith angle at Dome C is of about 50° at noon during Austral Summer). The maximum value of the downwelling irradiance is about $450\frac{W}{m^2}$, whereas it is about $370\frac{W}{m^2}$ for the upwelling one, both occurring in December.

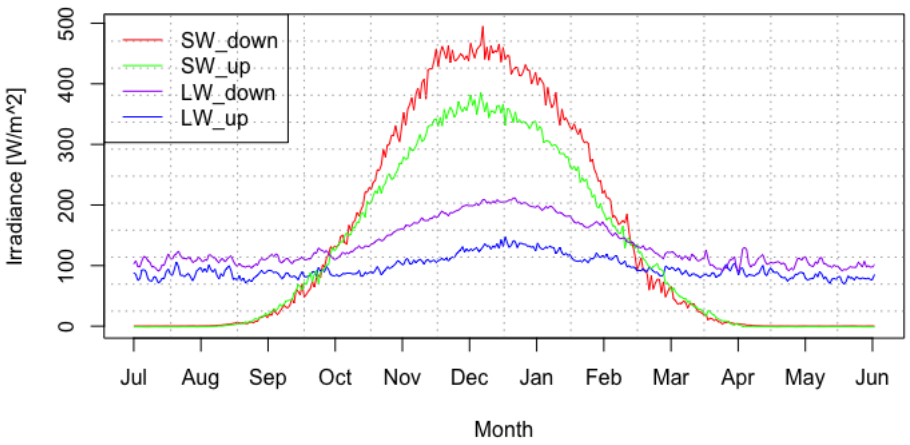

Figure 3.1: Monthly radiation in Antarctica

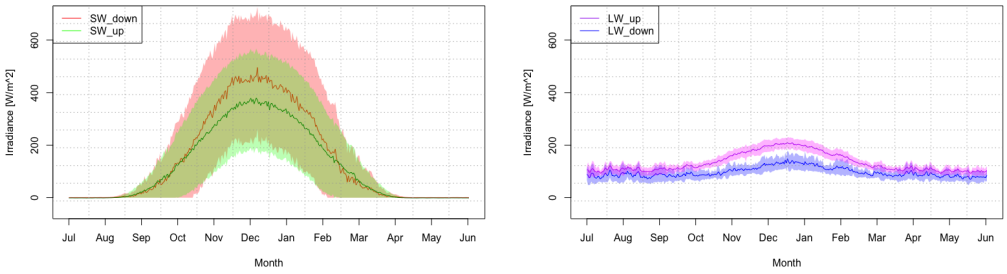

Figure 3.2: Standard deviations of shortwave and longwave components of radiation

The longwave upwelling irradiance is the radiation emitted by the snow surface. It is never zero and assumes an almost constant value of $100\frac{W}{m^2}$ from the beginning of April to the middle of September, when the system is not affected by the solar heating and surface temperature is nearly constant (see figure 3.1); from October to December its average value increases to $200\frac{W}{m^2}$ and then decreases again. The longwave downwelling irradiance, i.e. the one emitted by the atmospheric gases (in particular water vapour) presents more of less the same features of the upwelling one, remaining fairly constant around $90\frac{W}{m^2}$ during Antarctic Winter months and slightly increasing to a maximum of about $120\frac{W}{m^2}$ between December and January; this fact means that atmospheric temperature is not as sensible as the surface one to the Solar heating.

In Figure 3.2 it is possible to observe the standard deviations for the irradiance components. We can see that the standard deviation of the shortwave irradiance is way bigger than the one of the longwave irradiance. This is due to the greater influence of clouds on the solar radiation then the Earth one. During winter months there is the opposite beahviour because the shortwave radiation is null.

The monthly behaviour of the shortwave irradiance [Figure 3.3] does not present features different from the already described ones: maxima of around $450\frac{W}{m^2}$ for the downwelling and of around $350\frac{W}{m^2}$ for the upwelling irradiance. They always occur in December. The yearly trend for $F_{\downarrow,SW}$ oscillate between $100\frac{W}{m^2}$ and $200\frac{W}{m^2}$. For what concerns the yearly $F_{\downarrow,SW}$ it remains fairly constant around $150\frac{W}{m^2}$ for the whole period.

The behavior of $F_{\downarrow,LW}$ is the most interesting as it presents a rise of about $30\frac{W}{m^2}$ from 2010 to 2020.

The last plot of $F_{\uparrow,LW}$ presents a smaller increment throughout the years, oscillating between $90\frac{W}{m^2}$ in colder months and 200 $\frac{W}{m^2}$ in warmer months. A slight increase is visible in the last 2 years.

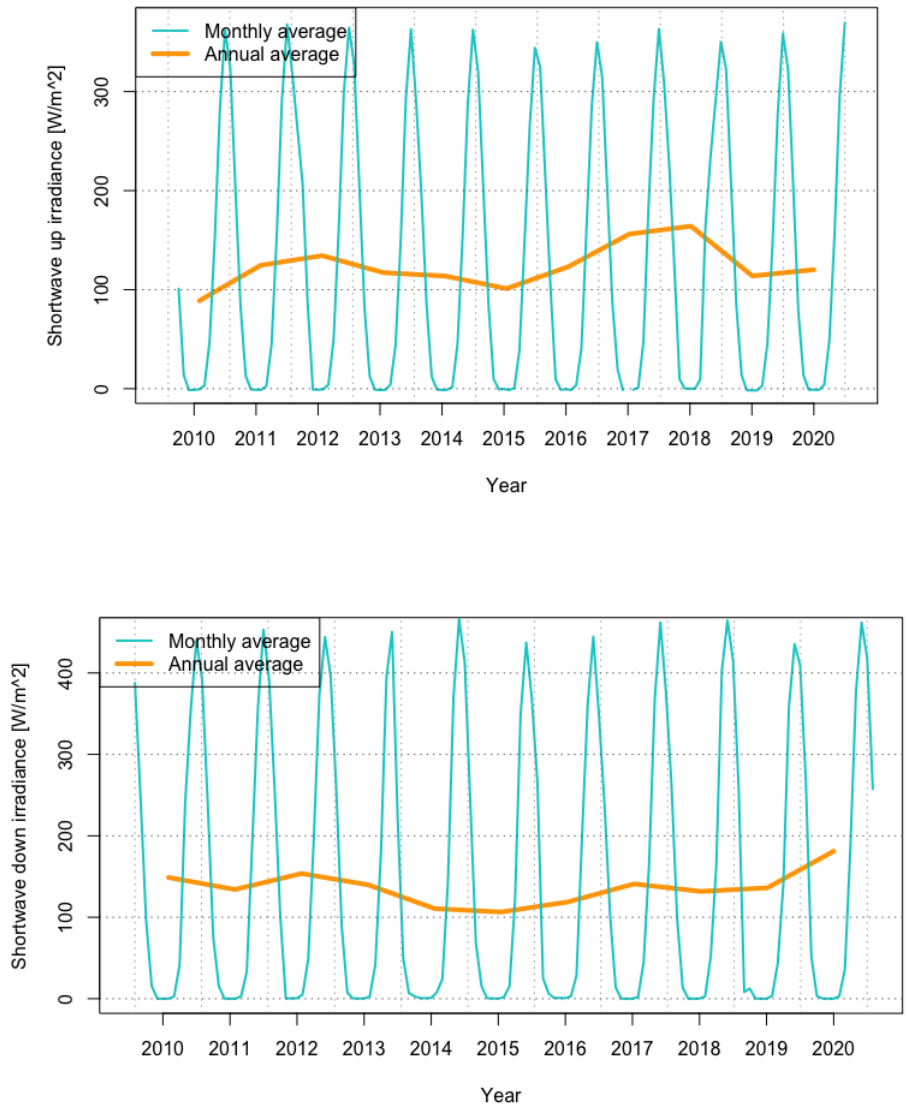

Figure 3.3: Mean annual and monthly shortwave upwelling radiation,shortwave downwelling radiation.

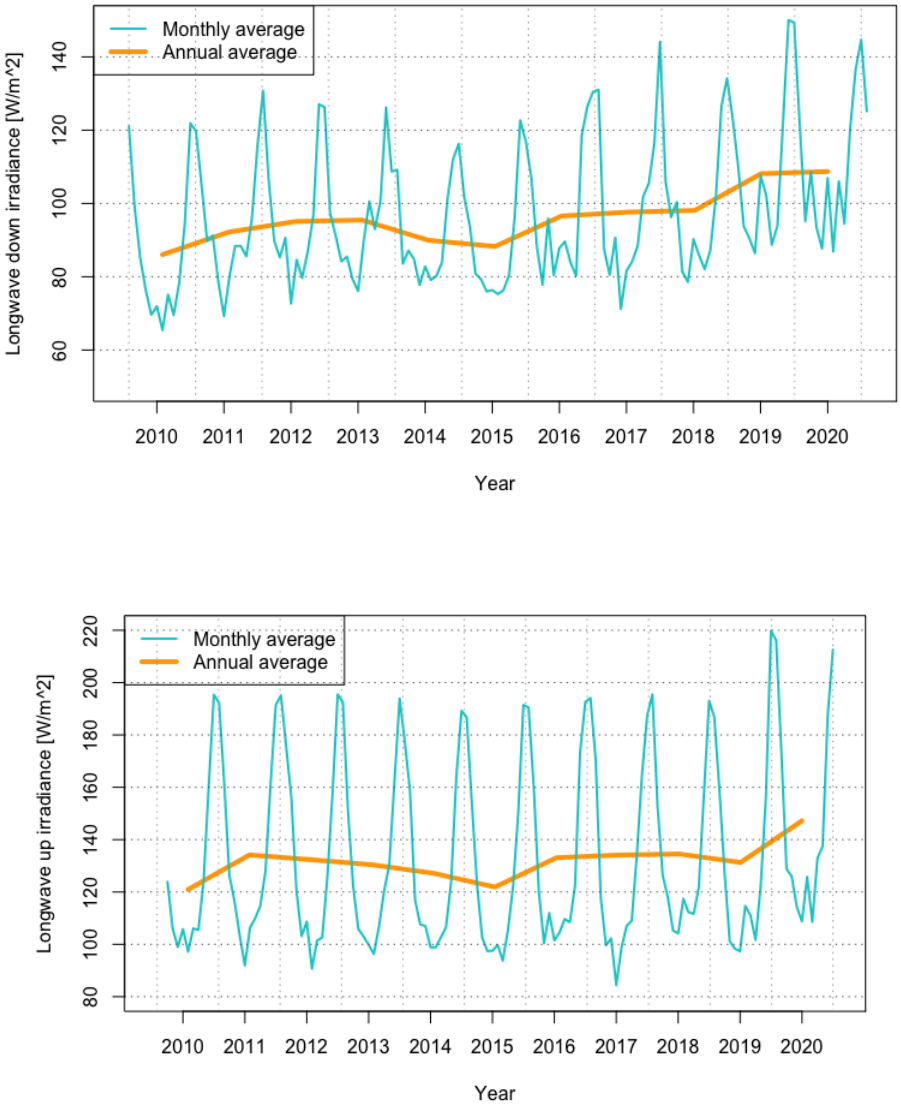

Figure 3.4: Mean annual and monthly longwave upwelling radiation and longwave downwelling radiation

As seen in [16] it is useful also to plot the radiation as a function of hours and days. In Figure 3.5 is possible to observe the months-hour graph of the shortwave downwelling irradiance. This graph is useful to observe the general behaviour in the Dome C area for over a year. As already observed, the radiation distribution as a peak at the end of December, coinciding with the winter solstice. The graph represents the mean value of the values of every year for the entire decade. In this way we can reduce the noise.

3.2 Albedo in Antarctica

As a preliminary test we analyzed the snow albedo for shortwelling irradiance in Antarctica for January 2011 [Figure 3.6]. The showed behaviour is characteristic of all the Austral summer months with a mean value around 0.83 and a daily fluctuation of 0.05. In the antarctic winter month it is not possible to make this kind of calculation due to the absence of downwelling shortwaves radiation.

After the albedo of January 2011 we made a zoom on the daily variation in the same period [Figure 3.7]. It is possible to see that the albedo oscillates between 0.8, in the night and in the evening, and 0.9 in the afternoon.

3.3 Clear sky analysis

3.3.1 Detection methods

Cloudy sky exhibits shortwave features that clear sky does not, which can be used to separate the two situation within the dataset. Four tests are used to eliminate data that occur under cloudy skies.

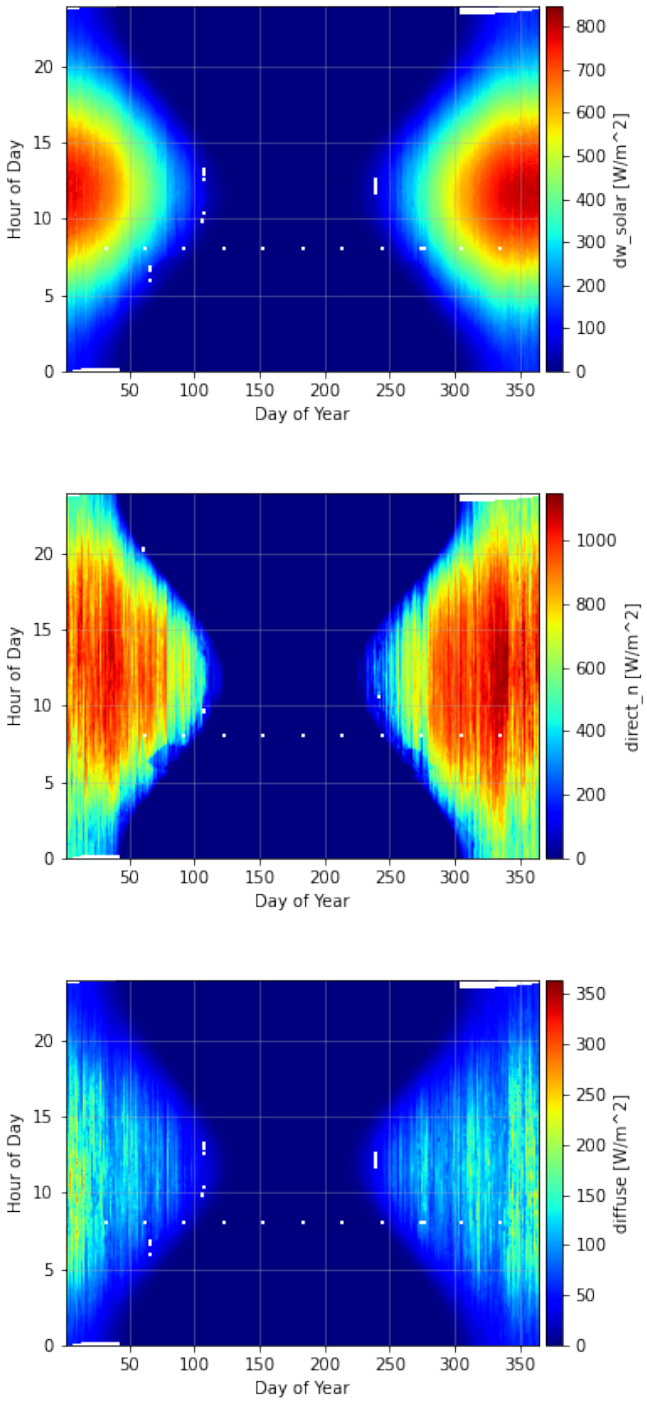

Figure 3.5: Shortwave downwelling radiation components distribution [global (up), direct (center) and diffuse (down)] at Dome C

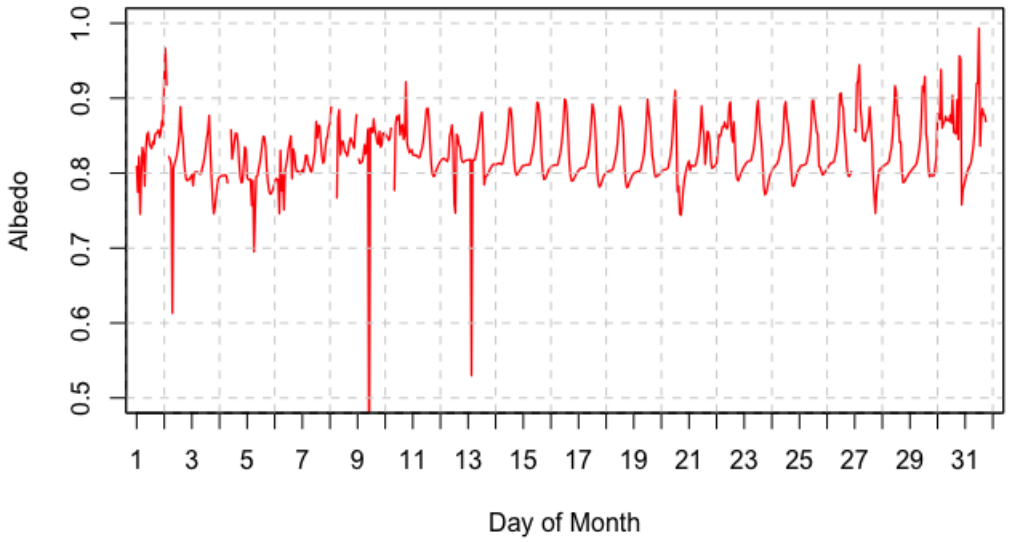

Figure 3.6: Albedo at Dome C in january 2011

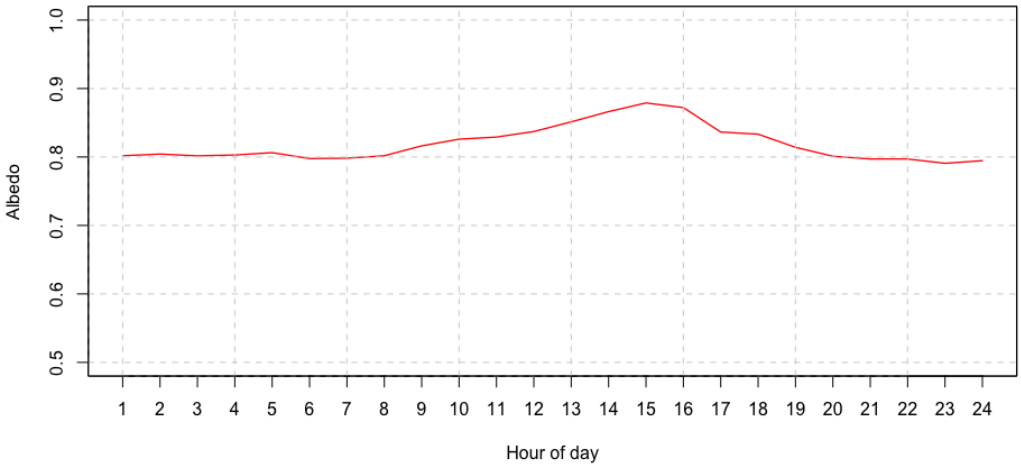

Figure 3.7: Mean daily Albedo at Dome C in january 2011

The first test ensures that the normalized total shortwave irradiance ($F_N = \frac{F}{\mu}$, where $\mu = cos\theta$) falls inside a certain range: maximum and minimum limits are set according to the characteristics of the measurement site. In this way obvious periods of cloudiness are eliminated, along with data at solar zenith angles greater than approximately 80° (for the $\mu = cos\theta$ normalization).

The second test concerns the diffuse component of the incoming radiation, that significantly increases in presence of clouds. A limit is imposed to the clear sky diffuse irradiance, so that it matches the tipical climatological value of the instrument location: all the data that fall above this limit are then eliminated. This test detects obvious periods of cloudiness, including or not thick haze or subvisual cirrus clouds, depending on the operator choice of the limit.

The third test checks the temporal change of the total shortwave irradiance: for clear sky this change is small over short periods of time with respect to changes due to cloud effects. The value $\frac{\Delta F}{\Delta t}$ is compared to the change of the top-of-atmosphere irradiance which reaches its maximum at $\theta = 90°$: based on this, a validity range is defined, so that only values falling in it are kept. This test is helpful in maintaining high solar zenith angle data (usually eliminated by the first test) because it considers that at longer atmospheric path lengths the insolation is small, so that $\frac{\Delta F}{\Delta t}$ is also small.

The fourth test uses the variability of normalized diffuse ratio (defined as the diffuse shortwave irradiance divided by the total shortwave irradiance, normalized with μ) to detect optically thin clouds: in fact this parameter is sensitive to small changes both in the diffuse and direct shortwave components. Authors point out the importance of the choice of the limit for clear sky running standard deviation of normalized diffuse ratio, because it strongly influences the number of data detected as clear: too low values cause an underestimation (interpreting system noise as cloudy conditions),

Minimum number of 1-min data detected as clear in a diurnal cycle for that day to be used for the fitting	90
Number of minutes of data for the running standard deviation used to detect clear sky	11
Normalized diffuse ratio standard deviation limit	0.0012
First guess of b parameter (typical average)	1.12
Low limit for total SW irradiance $[\frac{W}{m^2}]$	1
Clear-sky maximum limit for diffuse irradiance $[\frac{W}{m^2}]$	200

Table 3.1: Values used in the clear sky detection algorithm

and vice versa. They find that values between 0.001 and 0.0015 work well for the majority of the systems.

The tests' tresholds [17] are listed in table 3.1. .

Only data that pass all the tests are classified as clear and are used in the next step. It must be pointed out that measurements that meet all specified requirements are deemed representative of clear-sky measurements for a field of view of 160° , not 180° , because of the cosine response error of the instruments that increases with solar zenith angle: we will see that this limitation represents a problem for clear-sky detection in particular during last-first sunrise months (August/September and April), when solar zenith angles are higher than 80° .

3.3.2 Theoretical results

The primary factor that determines the magnitude of the diurnal cycle of downwelling shortwave irradiance for clear sky is the solar zenith angle. Long and Ackerman [17] found that a simple power law equation in the form

$$Y = a\mu^b \tag{3.1}$$

well represents clear-sky conditions. Equation 3.1 can be written as

$$Y = S_0 AU a' \mu(\mu^{b-1}) \tag{3.2}$$

where $S_0 = 1367 \frac{W}{m^2}$ is the solar constant and AU is the Sun-Earth distance correction. This form evidences better the rough meaning of the terms a and b; according to the authors, a represents the clear-sky irradiace for $\theta = 0°$ and includes such effects as the aerosol and column water vapor amounts, the mean Earth-Sun distance, and radiometer calibration; b includes instrumental effects such as the radiometer cosine response.

Data identified as clear by the four tests are fitted using the equation 3.1. Daily coefficients for both total and diffuse component (and by subtraction for the direct one) can be calculated only if a sufficient number of clear-sky values spanning a significant range of solar zenith angles is found on that day. A minimum number of identified clear-sky measurements for fitting has should be set; whether this requirement is never satisfied during the period (e.g. tropical climate sites which present persistent cloudiness or high latitude sites where the sun has a low elevation for the most of the day) an average value for the coefficients is estimated from the available data. When instead daily coefficients are determined for clear days, they can be linearly interpolated for cloudy days. Authors showed that ignoring ancillary input of the atmospheric state variables in operating the interpolation, produces uncertainties in the resulting irradiance within the estimated uncertainties of the radiometer used.

Obtained coefficients must meet some empirical constraints, otherwise are recalculated.

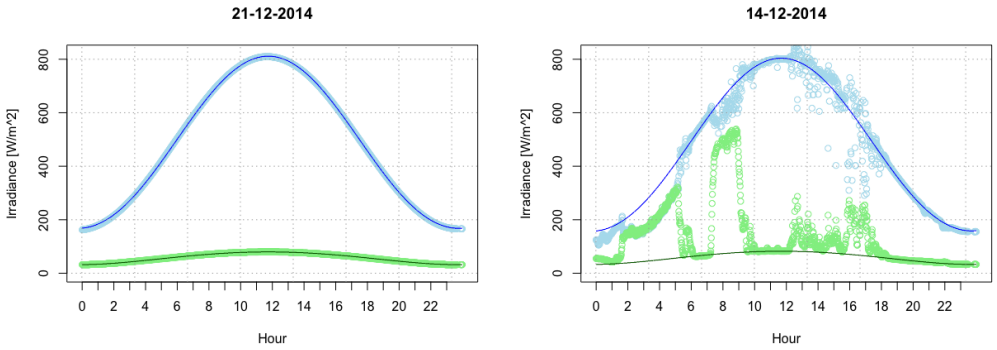

Figure 3.8: Direct and diffuse radiation in a clear day(left) and in a not clear day(right)

At the end of this step a series of daily coefficients a and b are available for the entire period, and are used to evaluate clear sky shortwave fluxes: these clear-sky values can be compared to the measured values to calculate the effect of clouds on radiation.

We show two examples of the result of the fit for global and diffuse irradiance for a cloudless day (21-12-2014) and for a partially cloudy day (21-11-2014) in figure 3.8 . Function 3.1 perfectly match the measurements in the first plot; in the second, negative cloud effect is evident for the global irradiance, whereas positive cloud effect occur in the diffuse component.

3.3.3 Cloudiness analysis

As an output of the algorithm we also obtain data useful to characterize the cloudiness of the site, such as the number of daylight minutes per day along with the number of detected clear sky data. We used these results to obtain a rough information about the cloudiness at Dome C, keeping in mind that bad data does not always correspond to cloudy sky.

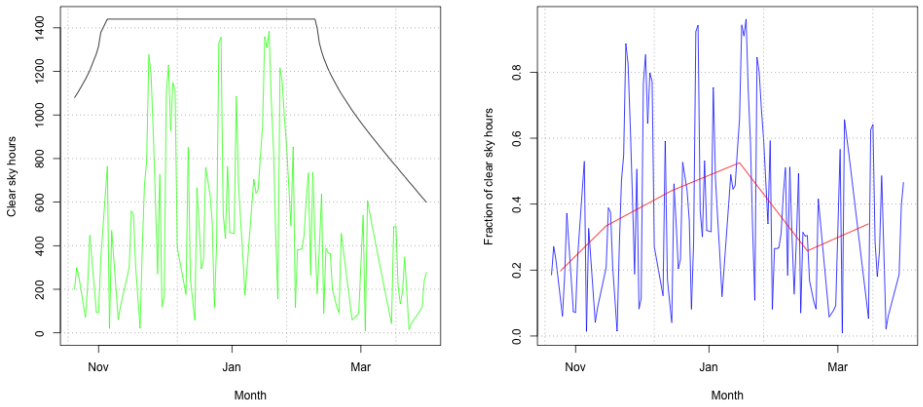

Figure 3.9: On the left image are represented clear minutes (in green) in antarctic summer between 2010 and 2011. In black total number of daylight minutes per day in the same period. On the right image is represented the percentage of clear moments in the same period. The blue line represents the daily trend while the red line represents the monthly mean

In figure 3.9 the daily number of total and clear-sky data are shown for the Antarctic summer 2010/2011. The maximum number of daylight minutes during summer months is 1440. Missing points are a consequence of the initial data quality check. From this plot we can get an idea of the general trend, namely a reduction of the relative number of clear-sky detected points per day during mid-seasons for all the years. Notice that no day was detected as completely cloudless, because the algorithm tends to eliminate low sun elevation measurements. This effect is enhanced at Dome C where maximum sun elevation is low during the major part of the year. The results for the remaining summer is in Appendix A.

In figure 3.9 is also possible to observe the percentage of clear moments for the Antarctic summer 2010/2011. The same analysis has been done for all the summer of the last decade. The results are listen in the Appendix

3.4 Coefficient analysis

We obtained a and b constants for every day for every summer day from 2010 to 2020. The algorithm fits the values for the global irradiance and for the diffuse irradiance, creating 2 different files. According to Long and Ackerman [17], a accounts for atmospheric effects and b for instrumental errors. However this separation is not so sharp. In fact, if a represents the attenuation of the radiation due to atmospheric absorption, it must be a function of the solar constant, the Sun-Earth distance, the latitude, water vapor and ozone content; we include these quantities in the definition of effective transmittance t(μ):

$$t(\mu) = \frac{a\mu^b}{S_0 AU\mu} \tag{3.3}$$

In figure 3.10 it's possible to observe the scatter plot a vs b and the approximate linear correlation between the 2 parameters; t(μ) represents the attenuation of solar irradiance due to atmospheric gases absorption, as it is the ratio of fitted ground irradiance (that for clear days is equal to the measured one) and theorical top-of-atmosphere irradiance.

In addition we computed the frequency histograms of the coefficients to analyze their behavior, both for the global and diffuse irradiance. Results are shown in figures 3.11 and 3.12. The histograms of a and b, for both global and diffuse radiation are similar, with an narrow peak above the mean value. The similarity in a and b distribution are a further confirmation of the linear correlation of the 2 values.

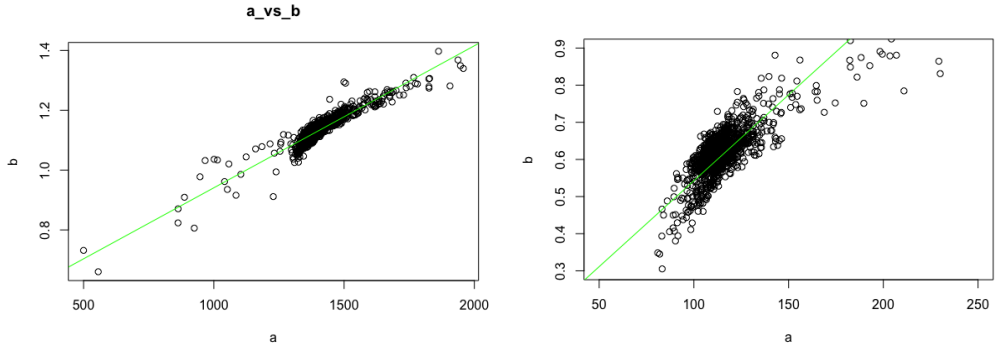

Figure 3.10: Linear correlation for A and B for global (left) and diffuse (right) radiation

.

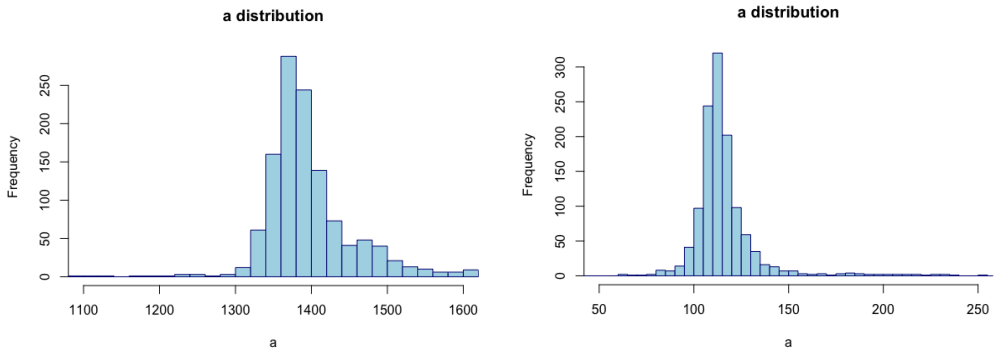

Figure 3.11: "A" distribution for global (left) and diffuse (right) radiation.

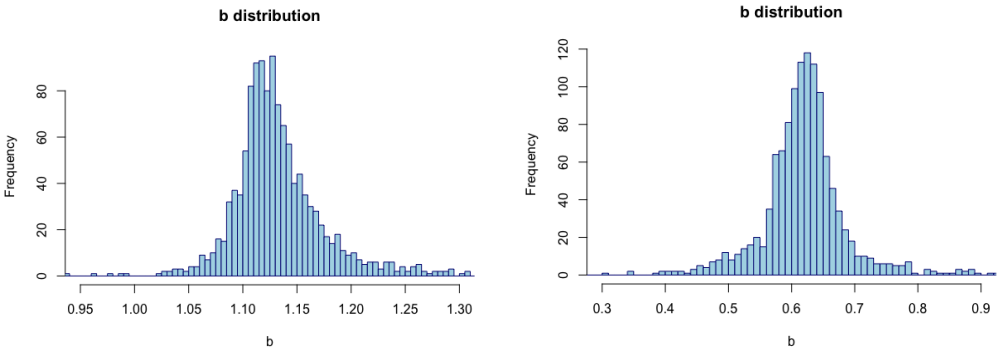

Figure 3.12: "B" distribution for global (left) and diffuse (right) radiation.

Chapter 4

Cloud Radiative Forcing

4.1 Shortwave irradiance

We define the cloud forcing on the shortwave downwelling irradiance as:

$$CF_{\downarrow,SW} = F_{\downarrow,SW,measured} - F_{\downarrow,SW,clear} \tag{4.1}$$

where $F_{\downarrow,SW,clear}$ ("clear" stands for clear sky conditions) are given by the Long-Ackerman clear-sky algorithm [17], and the normalized cloud forcing on the shortwave downwelling irradiance as:

$$CF_{\downarrow,SW,N} = \frac{F_{\downarrow,SW,measured} - F_{\downarrow,SW,clear}}{F_{\downarrow,SW,clear}} \tag{4.2}$$

We computed these quantities for the global and the direct component of the solar irradiance, to estimate the cloud effect on radiation during the day. Then we calculated the monthly averages.

The normalized cloud forcing is calculated to highlight the relative effect of clouds on the incoming radiation (a CF of $-50\frac{W}{m^2}$ is not as significant

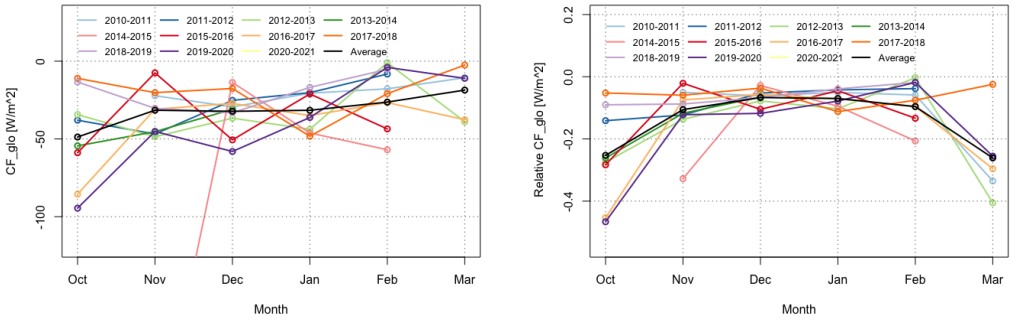

Figure 4.1: Monthly average of cloud forcing and normalized cloud forcing for the shortwave global irradiance. Colorful lines are referred to the different years, black line is the mean of all the decade

in January as it could be in September because total incoming radiation is lower in magnitude). Cloud Forcing is always negative, as it is expected, resulting from an attenuation of the direct irradiance on one side (negative cloud effect) which is stronger then the enhancements (positive cloud effect). For what concerns the mean, a minimum of $-50\frac{W}{m^2}$ is found in January, with a symmetric trend in the surrounding months 4.1. It is also possible to observe an apparent raise in the cloud forcing values during the summer. This behavior, however, disappers in the normalized graph.

For what concerns the mean, a maximum of $-0.05\frac{W}{m^2}$ is found between December and January, with a symmetric trend in the surrounding months.

All these average results present high standard deviations due to the daily variability of the quantity that we are considering. Nevertheless the possible to observe quite the same trend for the all the year of the last decade.

For what concern the diffuse shortwave radiation [Figure 4.2] we can observe an absolute value over $-10\frac{W}{m^2}$ for all summer months except for March. On the other side, if we consider the relative radiation, the exceptionality of March is less visible probably due to the fewer day of light in this month.

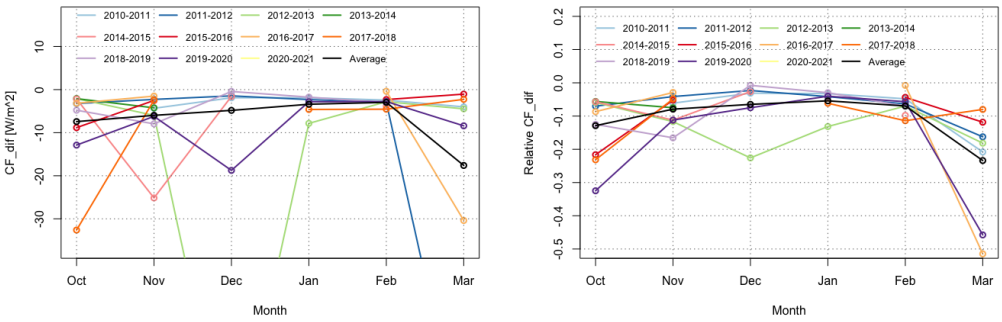

Figure 4.2: Monthly average of cloud forcing and normalized cloud forcing for the shortwave diffuse irradiance. Colorful lines are referred to the different years, black line is the mean of all the decade

Chapter 5

Conclusions and Future developments

In this thesis I have worked with different programming languages. Python as been used in the graph of the quality check [Figure 2.6] and in the months-hour graph of the shortwave downwelling irradiance [Figure 3.5]. All the other graphs have been made using R. The choice of the programming language has been made from time to time to obtain the best representation in the shortest possible time for every graph. This alternation in the use of languages has made it possible to obtain a clear and clean analysis of the radiative balance of the East Antarctic plateau.

In the past, many investigations on the Antarctic continent were conducted to calculate the cloud radiative forcing [i.e. [18],[19],[20]], but the majority of the stations are on the coast. This led to a shortage of data of the Plateau. This thesis has made an effort to close this gap.

The methods used in this thesis were based only on radiation data. This, taking into account the difficult conditions of the region that do not always enable an exact measurement of atmospheric data (such as temperature and

humidity profiles), can be a great benefit for future studies. Nevertheless the treatment of low sun elevation data still requires some adjustments, and a comparison with other cloud detection techniques should be carried out for a better tuning of the parametric representations of cloudfree sky.

Studies on the radiation budget in Antarctica con provide a useful tool for the future development of a solar farm in the continent. During the summer Antarctica recieve 24 hours of sun light. This can be a valuable resource as renewable energy. The australian governament has already taken some steps in this sense [21], but lots of research still needs to be done.

This work is only based on radiation data, so that every quantity obtained does not require the knowledge of additional informations. Considering the harsh conditions of the area that do not alwas allow an accurate measure of atmospheric parameters (such as temperature and humidity profiles), the methodology proposed can be an useful and simple tool to calculate the CRF.

Some adjustements are still needed though, in particular for the treatement of low sun elevation data; furthermore, a comparison with other cloud detection methods should be performed for a better tuning of the parametric representations of cloudfree sky.

Bibliography

[1] Wallace J. and Hobbs P. *Atmospheric Science: An Introductory Survey II.* Academic Press, 2006.

[2] J.J. Carroll and B. W. Fitch. Effects of solar elevation and cloudiness on snow albedo at the south pole. *Journal of Geophysical Research: Oceans*, 86(C6):5271–5276, 1981.

[3] Lord Rayleigh. On the electromagnetic theory of light. *Journal of Science*, 12 (73):81–101.

[4] G. Mie. Contributions to the optics of diffuse media, especially colloid metal solutions. *Ann Phys*, 1908.

[5] Salby. *Fundamentals of Atmospheric Physics.* Academic Press, 1996.

[6] G. G. Goyer and R. Watson. The laser and its application to meteorology. *Bulletin of the American Meteorological Society*, 44 (9):564–575, 1963.

[7] Harry D. Kambezidis. The solar radiation climate of athens: Variations and tendencies in the period 1992–2017, the brightening era. *Solar Energy*, 173:328–347, 2018.

[8] V.P. Walden M.S. Town and S. G. Warren. Cloud cover over the south pole from visual observations, satellite retrievals, and surface-based infrared radiation measurements. *Journal of Climate*, 20(3):544–559, 2007.

[9] T. Lachlan-Cope. Antarctic clouds. *Polar research*, 29(2):150–158, 2012.

[10] P. Ricchiazzi C. Gautier and D. Lubin. Cloud scattering optical depth and local surface albedo in the antarctic: Simultaneous retrieval using ground-base. *Journal of geophysical research*, 100(D10):021–091, 1995.

[11] A. Driemel; et al. Baseline surface radiation network(1992-2017). *Earth Syst. Sci. Data*, 10:1491–1501, 2018.

[12] L. J. B. McArthur. Baseline surface radiation network (bsrn). *Operations Manual, WMO/TD-NO*, 2004.

[13] S. Wilbert D. Schüler R. Affolter B. Kraas E. Lüpfert B. Espinar N. Geuder, F. Wolfertstetter. Screening and flagging of solar irradiation and ancillary meteorological data. *Energy Procedia*, 69 (May):1989–98, 2015.

[14] C. A.Gueymard. Cloud and albedo enhancement impacts on solar irradiance using high-frequency measurements from thermopile and photodiode radiometers. part 1: Impacts on global horizontal irradiance. *Solar Energy*, 153 (September):755–65, 2017.

[15]

[16] Harry D. Kanmbezidis. The solar radiation climate of athens: Variations and tendencies in the period 1992-2017, the brithtening era. *Solar energy*, 173:328–347, 2018.

[17] C. N. Long and T. P Ackerman. Identification of clear skies from broadband pyranometer measurements and calculation of downwelling shortwave cloud effects. *Journal of Geophysical Research: Atmospheres*, page 15609–15626, 2000.

[18] A. Lupi M. Nardino V. Vitale, c. Lanconelli and T.Georgiadis. Estimation of fractional sky cover, cloud type and cloud forcing effects at terra

nova bay from broadband radiation measurements. *Italian research on Antarctic Atmosphere*, 2004.

[19] Vitale Georgiadis Calzolari Evangelisti Tomasi Bortoli Nardino, Lupi and Trivellone. Cloud effects on the radiative balance terms at terra nova bay. *Italian research on Antarctic Atmosphere*, 2002.

[20] Trends in cloud amount and radiative fluxes at syowa station, antarctica. *Polar Science*, 1(1):17–23, 2007.

[21] W. Pyper. Casey solar farm. *Australian Antarctic Magazine*, 36:12–13, 2019.

Appendix A

Cloudiness analysis

In the following graphs is possible to observe a rough estimation of cloudiness in Antarctica for the last decade. On the left side are listed, in green, the number daily number of clear minute with respect to the total, in black. On the right side the fraction of clar sky minutes is reported.

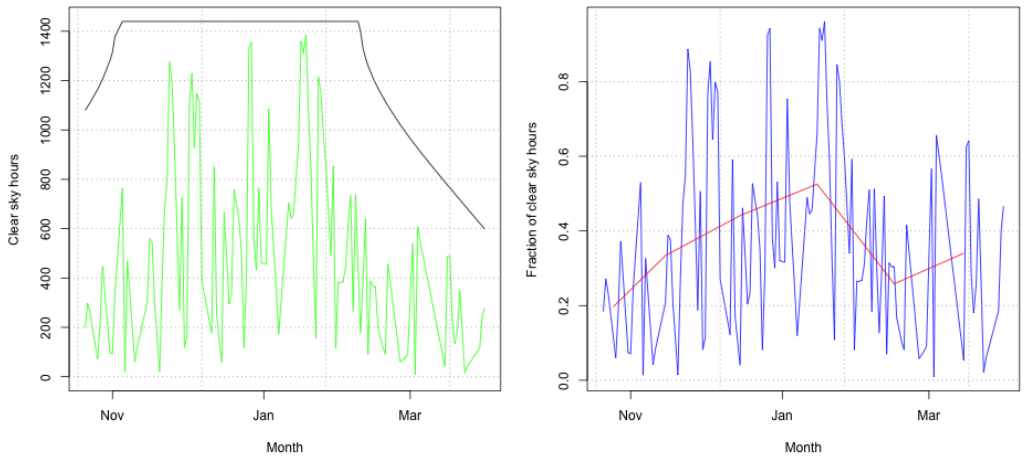

Table A.1: Number (left) and fractions(right)of clear sky hours in the 2010/2011 summer

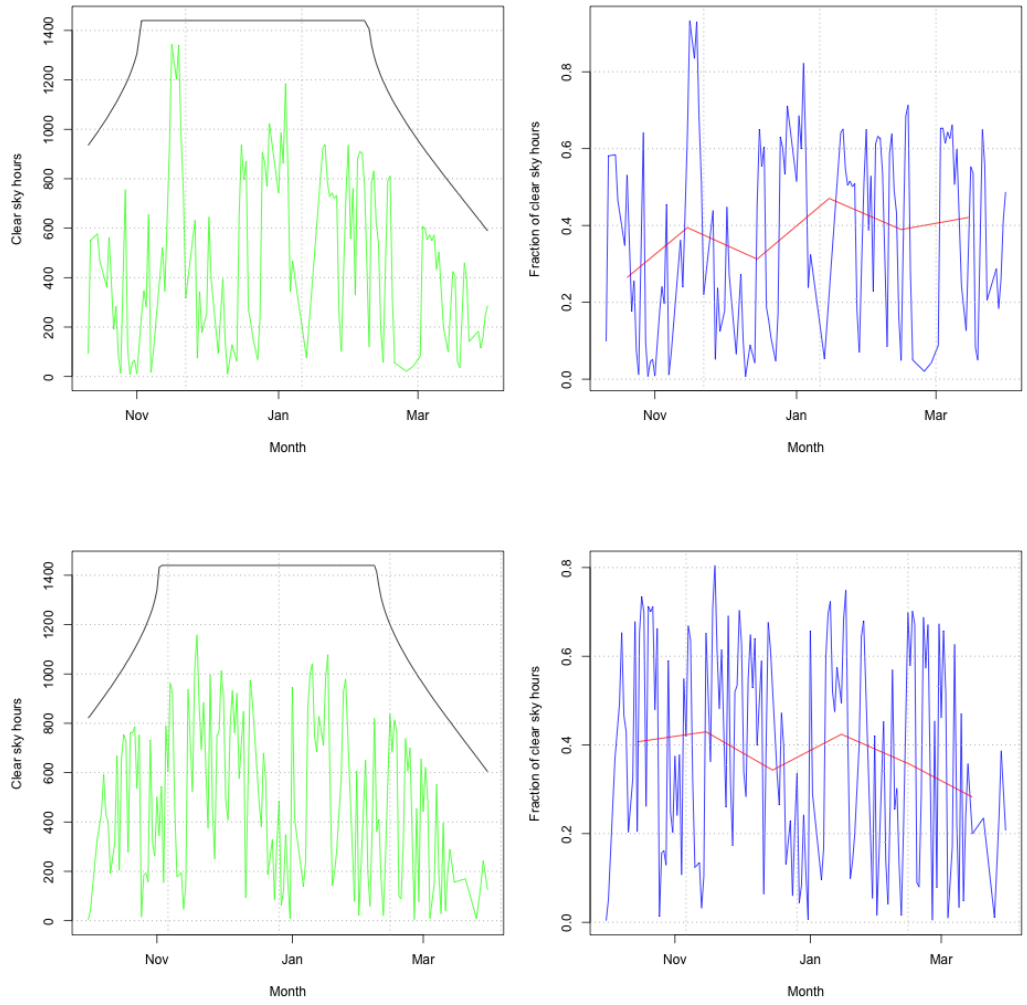

Table A.2: Number (left) and fractions (right) of clear sky hours in the 2011/2012 and 2012/2013 summer

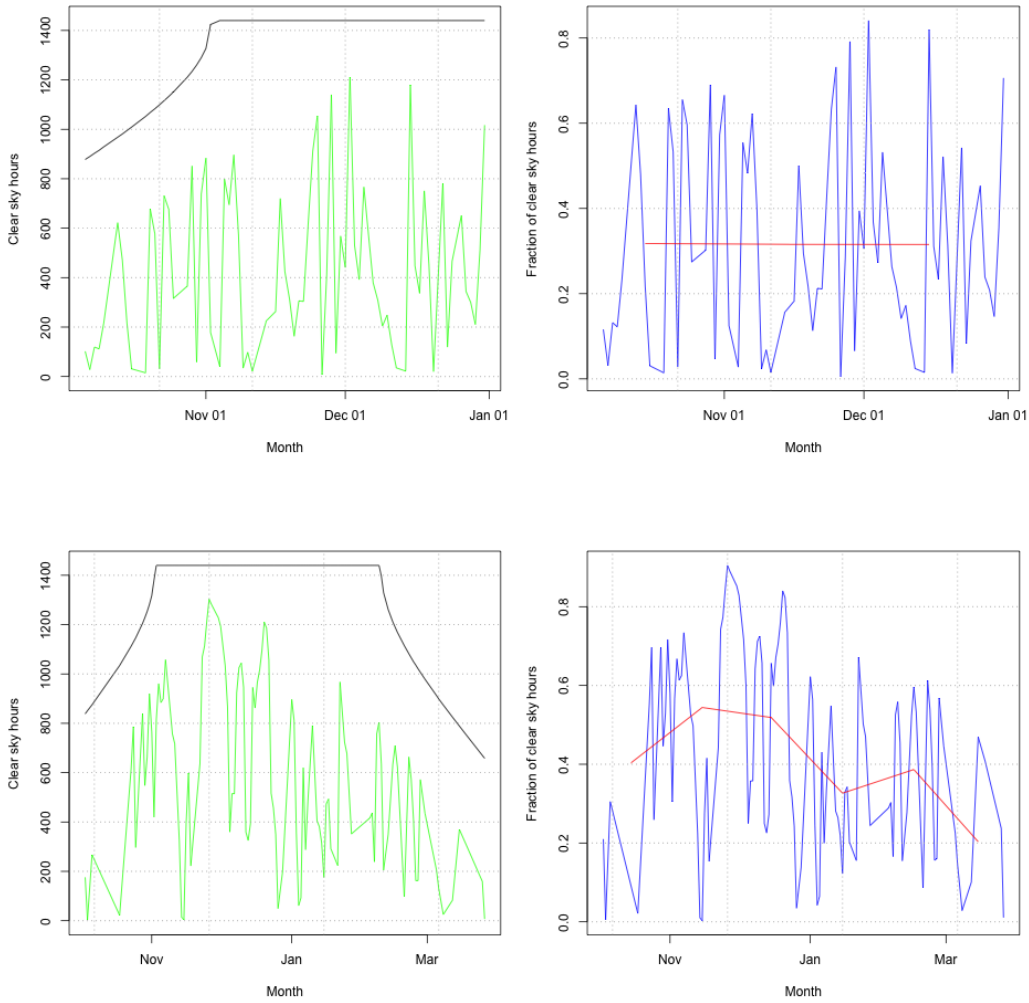

Table A.3: Number (left) and fractions (right) of clear sky hours in the 2013/2014 and 2014/2015 summer

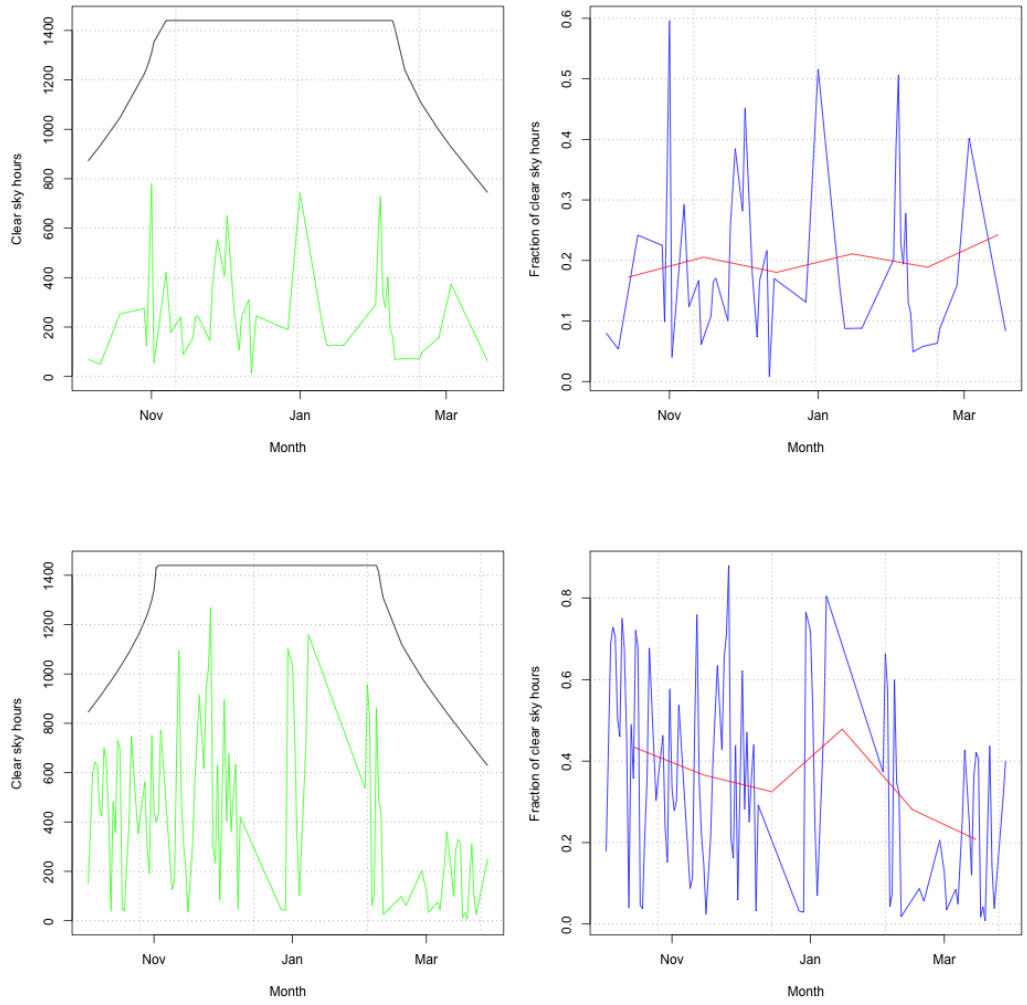

Table A.4: Number (left) and fractions (right) of clear sky hours in the 2015/2016 and 2016/2017 summer

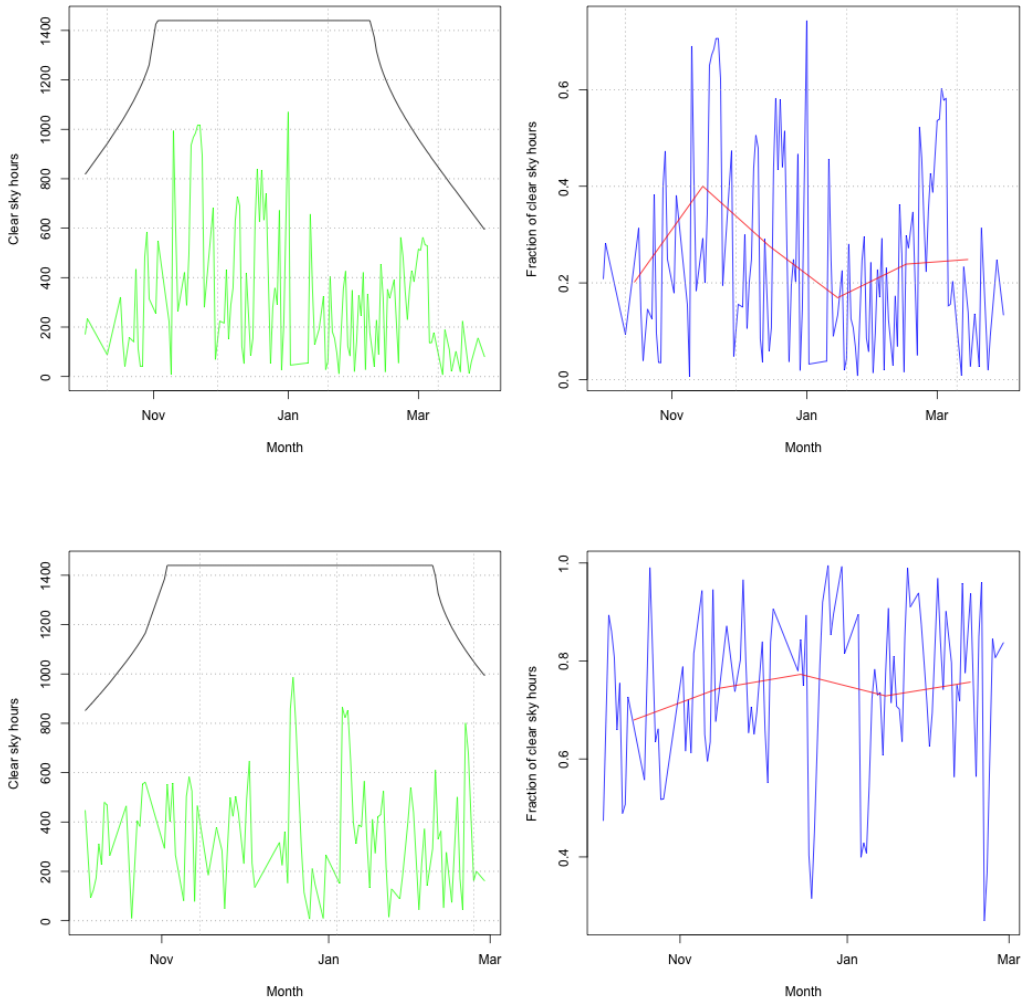

Table A.5: Number (left) and fractions (right) of clear sky hours in the 2017/2018 and 2018/2019 summer

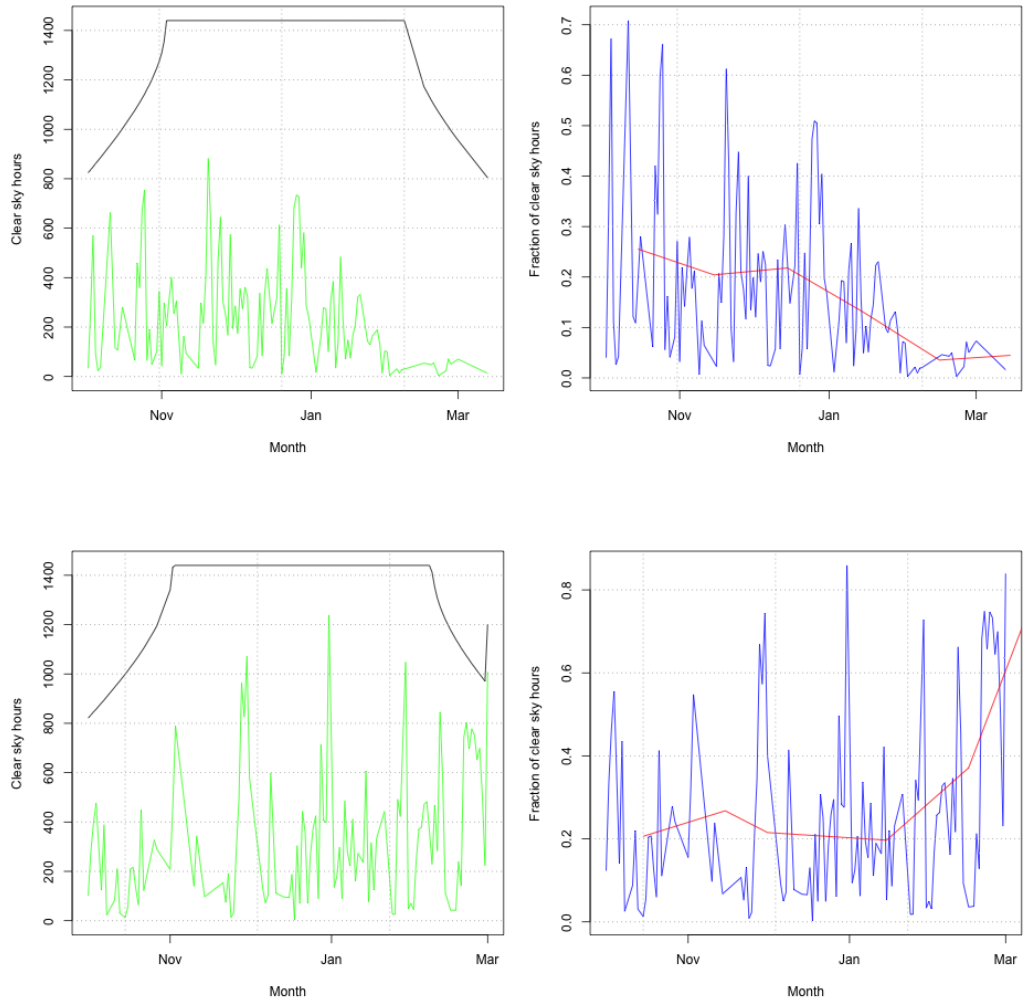

Table A.6: Number (left) and fractions (right) of clear sky hours in the 2019/2020 and 2020/2021 summer